Journal of the European Ceramic Society 42 (2022) 6703–6712

Contents lists available at ScienceDirect

Journal of the European Ceramic Society

journal homepage: www.elsevier.com/locate/jeurceramsoc

Comparison of in-situ oxidation behavior of Zr by micro-arc oxidation and selective laser melting

Wei Shao [a,b], Cancan Liu [c], Qiaojun Wu [c], Hongtao Li [b,c,*], L.A. Angurel [b,**], G.F. de la Fuente [b], Bailing Jiang [c]

[a] Institute of Welding and Surface Engineering Technology, Faculty of Materials and Manufacturing, Beijing University of Technology, 100124 Beijing, China
[b] Instituto de Nanociencia y Materiales de Aragón (CSIC-Universidad de Zaragoza), 50018 Zaragoza, Spain
[c] College of Materials Science and Engineering, Nanjing Tech University, 210009 Nanjing, China

ARTICLE INFO

Keywords:
In-situ oxidation
Zr coating
Micro-arc Oxidation
Selective Laser Melting

ABSTRACT

Al_2O_3-ZrO_2 ceramic coatings were prepared on 6061 Al alloy by Micro Arc Oxidation (MAO) and Selective Laser Melting (SLM). Coatings prepared by MAO exhibit a porous structure and a progressive oxidation of the substrate as a function of processing time. Those made by SLM are denser, although the presence of cracks is observed throughout their surface. XRD results suggest that the ceramic coating consists of m-ZrO_2, t-ZrO_2 and γ-Al_2O_3 phases for the MAO process, while a Zr_3O phase is also present in SLM. The hardness of the MAO Al_2O_3-ZrO_2 coating is higher than that obtained by SLM. Young's modulus of the MAO coating is lower, due to higher level of porosity observed in the coating prepared by MAO. Moreover, in-situ oxidation, heating and solidification processes are all discussed and compared within the context of MAO and SLM peculiarities. The processes and transformation mechanisms involved in the processing methods produce diverse microstructures.

1. Introduction

Micro-arc oxidation (MAO) is an effective in-situ oxidation technique to fabricate metallurgical oxide coatings on the surface of valve metals (aluminum, magnesium, titanium, zirconium, etc.) and their alloys, utilizing a microarc discharge generated by dielectric breakdown [1–4]. Owing to the high temperatures achieved during the microarc discharge, atoms within the micro-zone of the substrate react with the oxygen plasma [4–7]. Aluminum alloys are a kind of valve metals which can be MAO processed to form an aluminum oxide coating. The coating can improve the mechanical and corrosion properties for applications in various industrial sectors such as aerospace, automotive, naval, biomedicine, electronics, or energy [8,9].

However, Al_2O_3 coating is not ideal for high-temperature applications because of its high thermal conductivity and poor thermal shock resistance [10]. A practical method to further enhance the mechanical performance of alumina is combining it with suitable materials such as ZrO_2, SiC or TiO_2 [5–9]. Among the alumina-based composites, the Al_2O_3-ZrO_2 system provides unique features. Zirconia is recognized as an interesting material in fundamental studies because of its good chemical and dimensional stability, high melting point, low thermal conductivity and high wear resistance. ZrO_2 has been widely applied in many fields, such as engine components, cutting tools, thermal barrier or wear-resistance coatings, as well as in biomedical implants [11].

On the other hand, selective laser melting (SLM) [12] has been often used for Laser Additive Manufacturing (LAM) of ceramics. It has also been used to densify and control the microstructure of oxide coatings on metallic substrates [13,14] and even achieve attractive Al_2O_3-ZrO_2 eutectic coatings [15,16]. The microstructure and properties of Al_2O_3-ZrO_2 coatings fabricated by MAO and SLM may expectedly be quite different. Therefore, it is of interest to compare the in-situ oxidation behavior of Zr (ZrO_2-based) coatings obtained via MAO and SLM.

In this paper, Al_2O_3-ZrO_2 coatings are thus fabricated by two promising methods, MAO and SLM, through a pre-deposited Zr coating on the substrate. The outcome allows a systematic comparison of the morphology, microstructure and phase composition of the Al_2O_3-ZrO_2 coating after different in-situ oxidation processes. It is expected that the detailed behavior of in-situ oxidation upon heating, melting, and directional solidification, can be illustrated in a straightforward way. This is of significance to pave the way towards the scalable fabrication of

* Corresponding author at: Instituto de Nanociencia y Materiales de Aragón (CSIC-Universidad de Zaragoza), 50018 Zaragoza, Spain.
** Corresponding author.
E-mail addresses: li_ht@163.com (H. Li), angurel@unizar.es (L.A. Angurel).

https://doi.org/10.1016/j.jeurceramsoc.2022.07.005
Received 18 April 2022; Received in revised form 4 July 2022; Accepted 6 July 2022
Available online 8 July 2022

functional materials based on Al_2O_3-ZrO_2 composite coatings, as well as to design a new coating process via in-situ oxidation techniques.

2. Experimental methods

2.1. Sample preparation procedure

Two different sets of samples have been fabricated using a multi step procedure. Fig. 1 shows a diagram of the two processes that have been used to prepare the samples presented in this work.

Group I: A thin uniform layer (about 4–5 μm in thickness) of Zr was deposited on bare 6061 aluminum alloy substrate by magnetron sputtering ion plating followed by oxidation via MAO.

Group II: A MAO process was applied initially to bare 6061 aluminum alloy substrates in order to obtain an Al_2O_3 coating. The latter was further coated with a Zr layer, deposited using magnetron sputtering ion plating. The sample surface was subsequently melted and directionally solidified via SLM.

The substrate selected in both cases was 6061 aluminum alloy, with the following nominal composition (mass fraction): 0.15–0.4 % Cu, 0.8–1.2 % Mg, 0.15 % Mn, 0.25 % Zn, 0.04–0.35 % Cr, 0.15 % Ti, 0.4–0.8 % Si, 0.7 % Fe and balance Al. Prior to surface treatments, circular specimens with a diameter of 35 mm and a thickness of 3 mm were ground successively with SiC papers up to 1500 grit, degreased with acetone, washed with distilled water and dried in a cool air stream.

Initially a MAO-50-II micro-arc oxidation apparatus (Nanjing HaoRang Environment Science & Technology CO. Ltd, China) was used to prepare a micro-arc oxidation Al_2O_3 ceramic coating with a thickness of 18 μm on the Al substrates of group II samples. MAO processing was carried out in 20 g/L Na_2SiO_4, 3 g/L Na_2WO_4 and 5 g/L NaOH solution under a DC pulse constant current mode, characterized by the following processing parameters: 4 A/dm^2, 500 Hz and 80 μs. The experiment was performed for a 30 min period. The solution temperature was kept below 30 °C during this MAO process. After this treatment, samples were rinsed with distilled water in an ultrasonic bath for 10 min in order to eliminate the effect of adsorbed solute anions.

These samples, with an Al_2O_3 coating, and a second set of 6061 substrates were prepared for depositing the Zr coating using a magnetron sputtering ion plating system (MSIP019). During the deposition process, the system was equipped with only one 330 × 135 mm vertically positioned magnetron installed in the chamber wall, and a 99.9 % pure Zr sputtering target (330 × 135 × 8 mm) was used. The substrate holder was designed to fix the substrate-to-target separation ($d_{s\text{-}t}$) at 120 mm with the rotation speed fixed at 5 rpm. Prior to deposition, the chamber was evacuated to a basic pressure lower than 3.0×10^{-5} Torr, and then backfilled with high purity argon (99.99 %) to the required depositing pressure (about 8.4×10^{-4} Torr), as measured using a capacitance manometer gauge. During the experiment, the Zr target current was fixed at 3 A during a deposition time of 30 min.

As illustrated in Fig. 1 for Group I samples, a final MAO treatment was performed to obtain the ceramic Al_2O_3-ZrO_2 coating. The MAO processing parameters applied for the latter were the same as for the preparation of the Al_2O_3 coating and deposition experiments were carried out during periods of 5, 15 and 30 min.

In the case of the Group II samples, laser treatments were performed in Beam Scanning configuration to infiltrate Zr into the Al_2O_3 coating using two different pulsed lasers. These included a ps UV and a ns n-IR Yb fiber laser. The UV laser (ROFIN-SINAR LASER, PowerLine Pico 10–355) emits at 355 nm, with a maximum power of 3 W, a pulse width of 300 ps and its beam has an elliptical shape with 2a = 34 μm and 2b = 29 μm. The nIR Yb fiber laser (JEANOLOGIA LASER) has a nominal power of 20 W, emits at a wavelength of 1070 nm with a spot size of 36 μm, and its pulse width may be selected between 4 and 200 ns.

2.2. Characterization methods

The surface and cross-section morphologies of both, the original samples, as well as the samples after in-situ oxidation treatment, were studied using field emission scanning electron microscopy (FESEM, Carl Zeiss MERLIN). The elemental composition of the different phases observed within the coatings was determined by energy dispersive spectroscopy (EDS INCA350 Oxford Instruments). Crystalline phase content within the coatings after in-situ oxidation were also analyzed by X-ray diffraction (XRD) using a CuKα anode configuration (voltage: 40 kV, current: 40 mA, scan speed: 10°/min, samplings pitch: 0.02°).

Nanoindentation tests were carried out using a Nano Indenter G200 system (Agilent Technologies Inc) on polished surfaces of samples 1#−5# shown in Fig. 1 at different stages of the fabrication process to evaluate their mechanical properties, including hardness and Young's modulus. The equipment monitored and recorded the dynamic load and displacement of the indenter. The tests were performed using a trigonal Berkovich indenter and fused silica for standard area-function calibration, maintaining a constant drift rate of 0.05 s^{-1} and a 5000 nm depth limit. The indenter was driven perpendicularly into the coating, then out of it, using the continuous stiffness mode (CSM). The strain rate, harmonic displacement and frequency were set at 0.05/s, 2 nm and 45 Hz, respectively. Each indentation experiment consisted of three steps: loading, holding the indenter at peak load for 10 s, maintaining a depth limit at 5000 nm, and unloading completely. The Poisson ratios of 6061 Al alloy, Zr layer and Al_2O_3-ZrO_2 coating were set as 0.33, 0.34 and 0.31, respectively, and the indentation tests were repeated ten times at different positions within the sample's surface.

3. Results and discussion

3.1. In-situ oxidation behavior during the MAO process (Group I)

As described in the previous section, in order to obtain a ZrO_2-Al_2O_3 composite layer on the Al alloy, a Zr coating was deposited by magnetron sputtering on the sample and then MAO was used to produce the co-

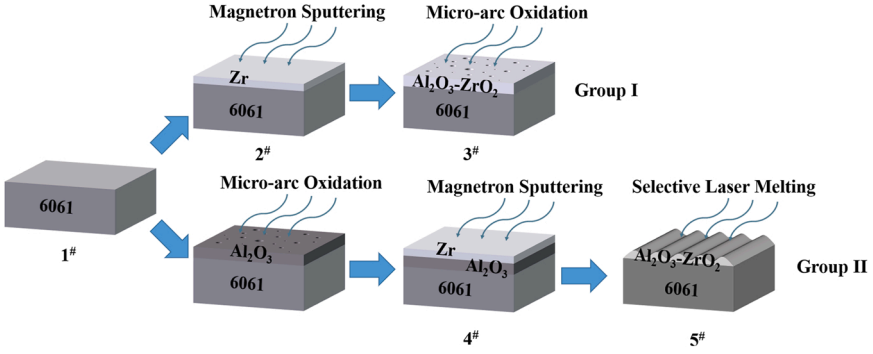

Fig. 1. Schematic diagram of the preparation of Al_2O_3-ZrO_2 layers by Micro-Arc Oxidation (MAO) and by Selective Laser Melting (SLM).

oxidation of both, the Zr layer and the substrate. Fig. 2 shows the voltage vs time response for this MAO process at a control mode of constant current density. During the first stage (I), the voltage increases from 0 V to almost 360 V in 1 min, promoting the formation of an insulating film (lower left inset) before the microarc oxidation starts. When the voltage is higher than the breakdown potential of the oxygen gas layer and the surface oxide layer, the sparks take place with formation of pores [17]. With continued oxidation, a transient period occurs, between about 360 V and 520 V, with a variable slope voltage-time response (stage II, center inset). Above 520 V, the voltage increases approximately linearly at a low rate up to a relatively stable value of about 560 V until the termination of the MAO process after 30 min (stage III, upper right inset).

The surface morphology and the cross-section aspect of the original Zr layer and of the coatings after 5- and 30-min MAO processes, are presented in Fig. 3. Elemental compositions of the observed phases were obtained by EDS and are indicated in Table 1. Observation of Figs. 3a-b thus indicates that the substrate is covered with a uniform ca. 4.50 μm thick, well-bonded Zr layer. Densely packed grains appear dispersed throughout the surface (Fig. 3a) and the cross-section (Fig. 3b) of this PVD coating, which exhibits a roughness value (R_a) of ca. 0.22 μm. This layer is the source of Zr during the subsequent MAO process. EDS measurements indicate that this original coating contains mainly Zr, accompanied by a small amount of oxygen, as expected from the oxygen affinity of Zr metal and probably incorporated during the sample preparation that is required for microscopy analysis.

After a 5 min MAO treatment, the composite coating exhibits a significant increase in porosity and the appearance of micro-cracks, as revealed in Figs. 3c-3d. These account for the observed coating thickness increase in Fig. 3d. In addition, some of the microcracks that are observed on the surface topography appear due to the thermal stresses generated during the fast melting and solidification phenomena characteristic to MAO. The presence of these pores is also reflected in an increase in Ra values, up to 0.91 μm. In the cross-section view presented in Fig. 3d, it is observed that an inner Zr layer with some dissolved O is left with a maximum thickness ranging between ca. 3.6 and 4.3 μm. Within several areas, this Zr layer has disappeared completely. An external, highly porous and consequently thicker ZrO_2 layer is also generated. Moreover, there appear many cracks parallel to the surface of the coating, which result from the stress caused by the expansion of Zr due to the absorption of oxygen, as well as by the phase transformation from Zr to ZrO_2 [18]. In addition, perpendicular cracks also appear and are related to the formation of channels induced by the presence of microcharges. In consequence, in this initial stage of MAO, where the process has been carried out for a period of 5 min, the external part of the original magnetron sputtered Zr layer has thus been modified to ZrO_2, absorbing a relatively high content of oxygen, reaching a value of 68 at. % in region 3 (Fig. 3d), according to Table 1. Consistent with these observations, it may be proposed that the ZrO_2 layer in Fig. 3d forms by subsequent further oxidation of the sputtered Zr metal deposit, via oxygen uptake from the surface in contact with the electrolytic medium during micro arc oxidation.

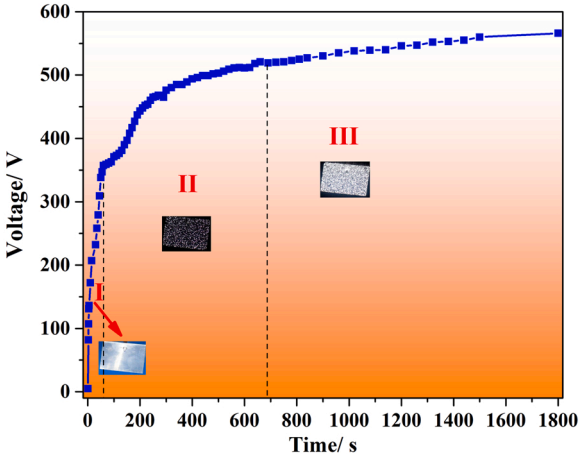

Fig. 2. The voltage vs time curve of MAO process at a constant current density $J = 4$ A/dm^2. The insets correspond to MAO stages I, II and III, as explained in the text.

In the case of the sample in which the MAO process extends during 15 min, the oxidation of the Al substrate to Al_2O_3 phase starts to take place once the Zr layer is depleted, as expected from its complete oxidation into ZrO_2. There appear two different ZrO_2 and Al_2O_3 layers with a distinct interface between them. The thickness of the external ZrO_2 layer ranges from 6.17 to 13.30 μm. In addition, the content of Al in the ZrO_2 layer ranges from 2.41 to 8.41 at. %, indicating that Al_2O_3 diffusion into the ZrO_2 layer has already begun.

When the duration of the MAO process is prolonged to 30 min, the number of pores on the coating surface that reach diameters larger than 5 μm increases (Fig. 3e), leading to a further increase in Ra, until a maximum value of 2.89 μm is reached. According to Fig. 3f, two layers are clearly identified within this coating. An external Al_2O_3-ZrO_2 layer appears above an inner Al_2O_3 layer. The thickness of the Al_2O_3-ZrO_2 layer ranges from 7 μm to 17 μm and that of the Al_2O_3 layer from 5 to 11 μm, both determined from the FESEM images presented in Fig. 3. When the MAO treatment reaches 30 min, the oxidized layer has already been transformed into an Al_2O_3-ZrO_2 phase, as determined by EDS on area 4 within Fig. 3f. Analysis on area 5 in the same Figure suggests, however, that further oxidation of the Al alloy substrate has taken place simultaneously to eutectic formation during this prolonged MAO process, yielding an intermediate layer of Al_2O_3 with a high level of porosity. Thus, as a result of longer MAO treatments, an outer surface Al_2O_3-ZrO_2 layer can be obtained in contact with an intermediate Al_2O_3 layer, which appears between the former and the Al alloy substrate.

According to the ZrO_2-Al_2O_3 phase diagram [19,20], the eutectic composition of Al_2O_3-ZrO_2 is about 63 mol. % Al_2O_3, corresponding to 29.6 at. % Al and 8.7 at. % Zr. In Fig. 4a, the composition of region 3 observed after 5 min transforms into the composition of region 4 after 30 min of MAO because of the melting of Al from the substrate during MAO. The latter composition (region 4) suggests the presence of the hypereutectic structure composed of Al_2O_3-ZrO_2 eutectic (67 mol. %) and primary Al_2O_3 (33 mol. %) grains. The high magnification micrograph shown in Fig. 4b displays the microstructure of the eutectic network of these two phases where ordered ZrO_2 lamellae are embedded within the Al_2O_3 matrix [21]. However, if the total amount of Zr deposited in the original MAO Zr layer is used to generate the eutectic, the expected thickness of the resultant Al_2O_3-ZrO_2 eutectic should be around 21 μm, which is larger than that of the experimentally observed thickness. Such a discrepancy may be due to the spalling of Zr, caused by the difference in the coefficients of thermal expansion between Zr and Al_2O_3 (Zr: $\sim 5.7 \times 10^{-6}$/K and Al_2O_3: $\sim 8.8 \times 10^{-6}$/K), and in part due to the cracks which appear parallel to the surface of the coating shown in Fig. 3d.

3.2. *In-situ oxidation behavior during SLM process (Group II)*

During laser processes, a large amount of energy is deposited in a localised region of the surface of the material during a very short time span. When the material is a metal with high thermal conductivity, the deposited energy spreads over a large volume. For this reason, SLM is not adequate to oxidize Al alloy underneath the Zr layer, as may be achieved with MAO. Group II samples thus have been prepared under a different configuration. Consequently, a metallic Zr coating was deposited by magnetron sputtering over an initial layer of Al_2O_3 fabricated by MAO. This 18 μm thick Al_2O_3 coating can act as a good thermal barrier towards heat loss to the Al substrate. In other words, it facilitates heat concentration within the sputtered metal layer. Fig. 5 shows FESEM

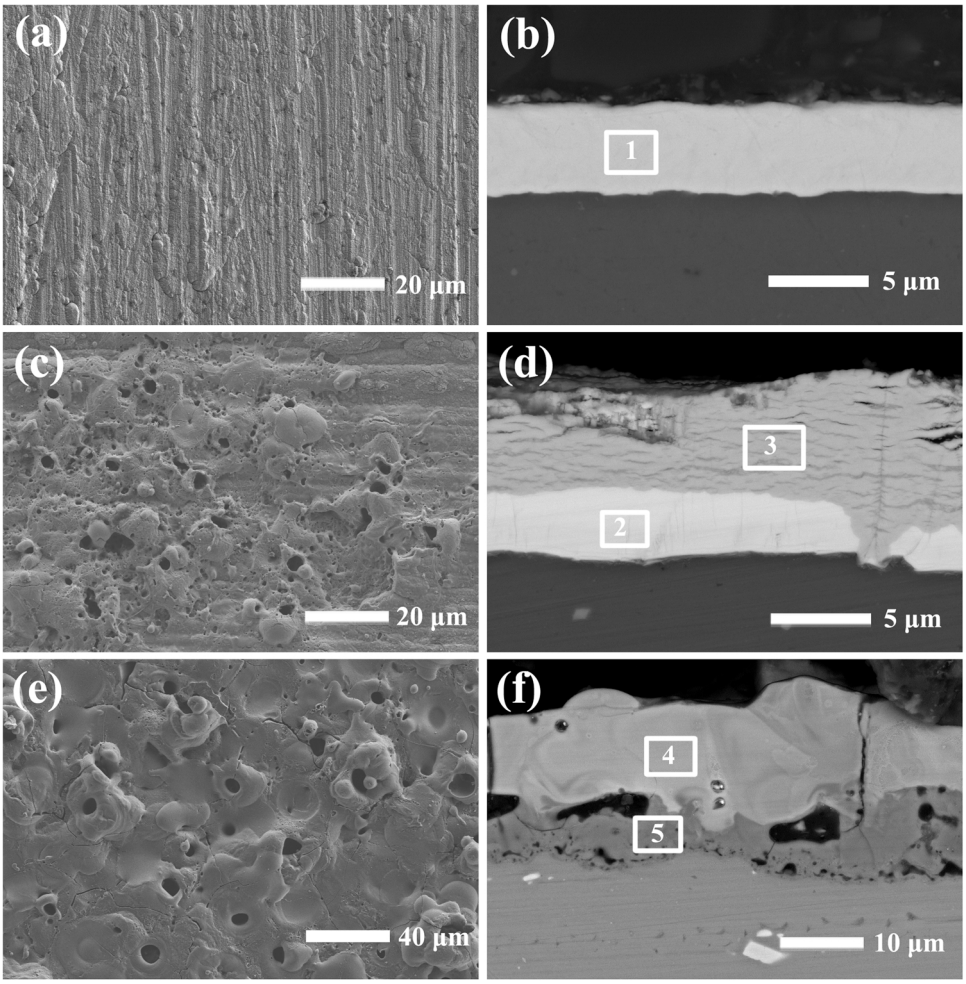

Fig. 3. FESEM images of surface and cross-section morphology of (a-b) the original Zr coating obtained by magnetron sputtering and the resultant Al_2O_3-ZrO_2 coatings developed during MAO after (c-d) 5 min and (e-f) 30 min periods. Numbered rectangles correspond to EDS analyses given in Table 1.

Table 1
Elemental composition (at. %) determined for the MAO coating phases found within the areas indicated in Fig. 3.

Site	O	Al	Zr
1	15.1	–	84.9
2	10.4	0.3	89.3
3	68.7	–	31.3
4	66.5	28.7	4.8
5	66.1	33.9	–

images of the surface and cross-section morphologies of the original Zr/Al_2O_3 MAO-produced coating. The composite coating exhibits some micro-pores and micro-cracks, as well as several large inner cavities. Fig. 5b reveals that Zr forms a uniform and well-bonded layer of approximately 4 µm in thickness with an Al_2O_3 layer of ca. 18 µm underneath. The Ra value of the coating reaches 1.88 µm. This high roughness value facilitates the laser processing because it increases the percentage of laser energy absorbed by the Zr metallic deposit [22,23].

The UV laser employed for this study emits within the sub-ns (300 ps) pulsed regime at a wavelength of 355 nm. It is expected to trigger mainly photochemical transformations on the irradiated surface, but due to the high laser frequency and its pulse width value approaching the ns regime it can also contribute to induce photothermal processes [24]. In consequence, it is expected that this laser treatment can induce thin molten layers with also limited thermal exchange towards the substrate. The laser parameters employed for this UV laser treatment are: average output power 2.9 W, pulse repetition frequency 300 kHz, laser scanning speed 50 mm/s, scanning line length 4 mm and distance between scanning lines 20 µm. Laser treatments were performed in air. The microstructure of the surface after the UV laser treatment is presented in Fig. 6. Using these laser parameters, the Zr layer is oxidized and melted, as a consequence of a predominantly photothermal process. The surface tension of the melt, combined with the laser beam displacement provoke the agglomeration of resolidified material into different size drops. It is clearly observed in the micrograph shown in Fig. 6a that the laser-remelted coating covers only part of the substrate surface, leaving significant areas exposed. From the cross-section morphology presented in Fig. 6b, it can be observed that the heat is sufficient to start to melt and mix the two oxides, although the amount of Al_2O_3 is not sufficient to obtain a uniform eutectic microstructure. In addition, the laser trace can be identified within these micrographs and will be discussed later on.

In order to prepare a more uniform remelted layer, a ns pulsed nIR laser was employed in order to increase the photothermal character of the laser-mater interaction and thus generate a larger molten volume and greater heat transfer to the coating/substrate system during the laser treatment. Fig. 7 shows the surface and cross-section morphologies of two coatings prepared using this ns nIR laser with two different sets of parameters. The laser treatment was performed in air with a pulse repetition frequency of 1 MHz, and an average power output of 12 W in both cases. In one of the samples, however, the laser beam scanned the surface at 400 mm/s with a distance between lines of 35 µm, while in the second sample these values were set at 150 mm/s and 5 µm,

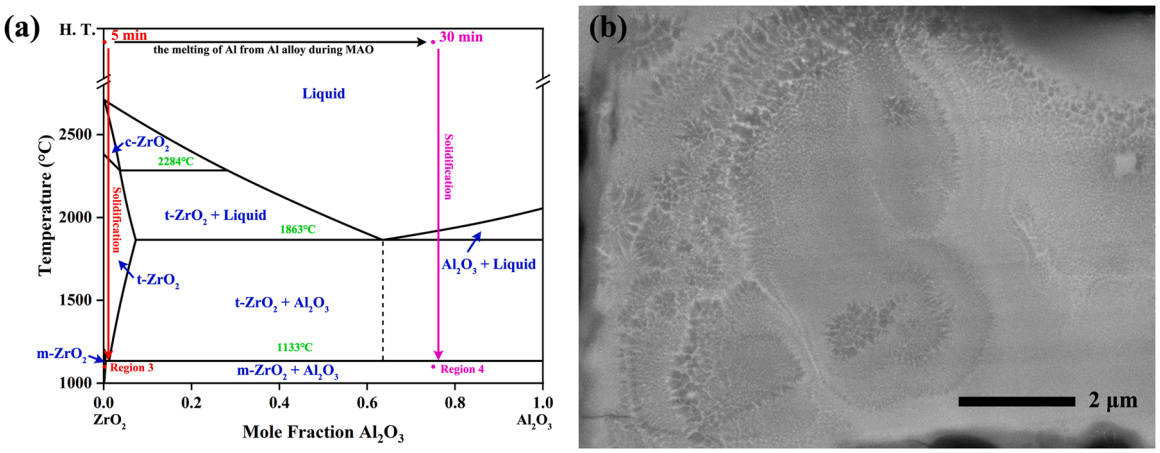

Fig. 4. (a) Transformation from ZrO_2 to Al_2O_3-ZrO_2 placed within the ZrO_2-Al_2O_3 equilibrium phase diagram after Ref. [20] and (b) microstructure of the eutectic Al_2O_3-ZrO_2 coating after a 30 min MAO treatment.

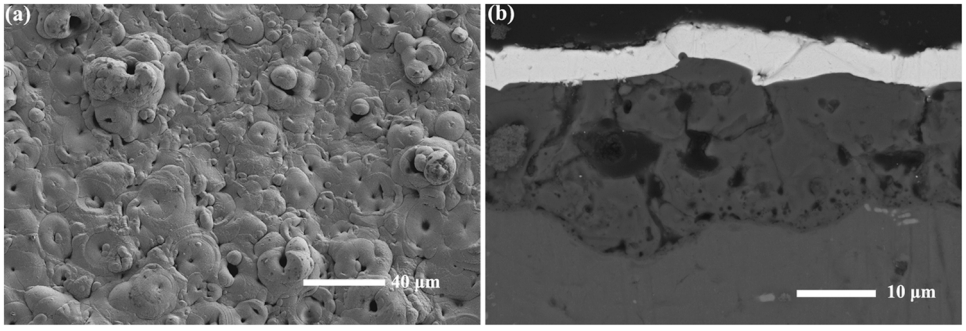

Fig. 5. Surface and cross-section morphologies of representative Zr/Al_2O_3 layer deposited by magnetron sputtering and MAO on 6061 Al alloy substrate.

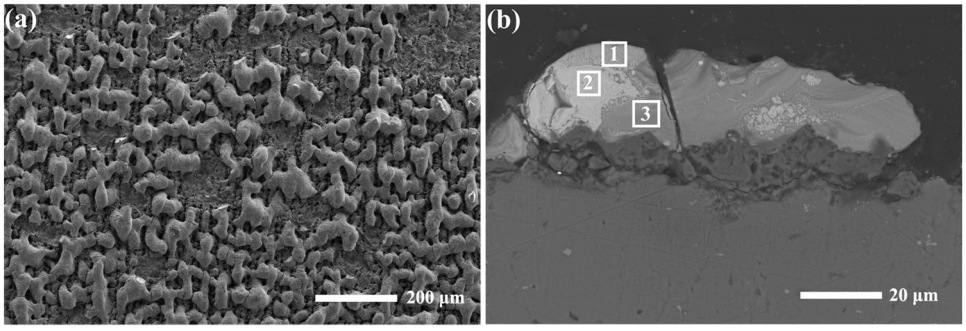

Fig. 6. Surface and transversal cross-section morphologies of Zr layer after sub-ns pulsed UV laser treatment.

respectively. These changes in parameters lead to a total average accumulated laser fluence [25] that is 19 times higher in the second treatment, in comparison with the first one. In both cases, scanning was performed in the vertical direction with respect to the orientation of the micrographs presented in Fig. 7a-b. Using the first set of parameters, the distance between laser scanning lines is larger than the size affected by the previous laser scan. Thus, the different lines scanned by the laser can be observed on the surface topography with a morphology that resembles semi-continuous lines, where surface tension accumulates the transient melt prior to solidification. In the second case, with a slower scanning speed and reduced line separation, the above coating morphology is replaced by a rough, porous surface. This cross-section exhibits an Al_2O_3-ZrO_2 structure where the different laser beam scan steps are observable, with a repeating line every 5 μm. It is also observed that cracks appear at some points, mainly at the interface with the Al substrate, and can propagate along the full thickness of the coating. These are likely due to high thermomechanical stress characteristic to laser processing of ceramics [26,27].

In the magnified Fig. 7e-f, the Al_2O_3-ZrO_2 layers appear to contain smaller grains with slower beam scan speed and smaller line-to-line scanning distance. The average laser energy density was defined in Ref. [28] as follows:

$$\mathrm{VED} = \frac{P}{vhd} \tag{1}$$

where VED is the volumetric energy density, P is the laser power, v is the scanning speed, h is the scanning hatching (distance between scan lines) and d is the thickness of the layer affected by the laser. According to the equation, the average laser energy density decreases with the larger scanning hatching and the faster scanning speed. The heat input melts

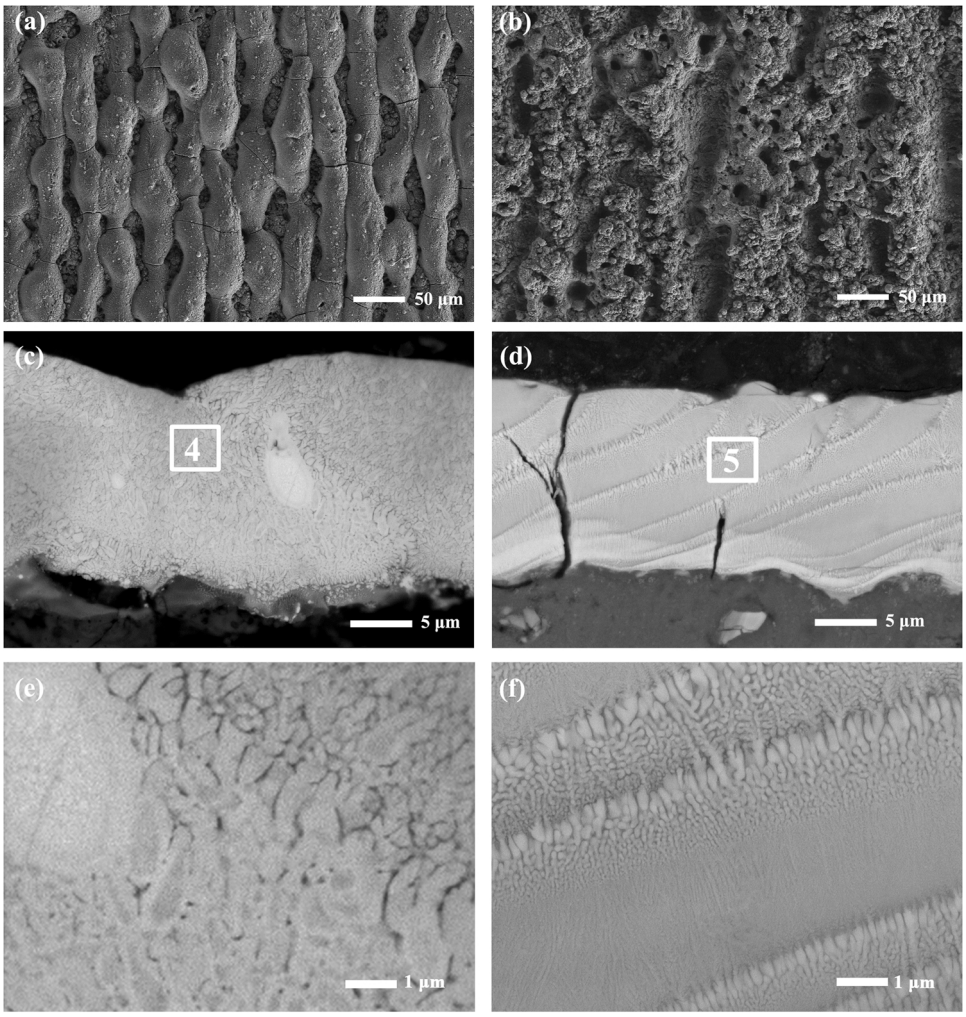

Fig. 7. Surface and cross-section morphologies corresponding to sputtered MAO coatings on Al alloy substrates after treatment with a near IR ns pulsed Fiber laser emitting with 12 W average power at a pulse repetition frequency of 1 MHz. Beam scan rates and line to line spacing was set at 400 mm/s and 35 µm in (a, c, e) and 150 mm/s and 5 µm in (b, d, f), respectively.

the coating creating an elliptical melt pool [29]. As the heat source is displaced, the melt pool rapidly solidifies. Its solidification microstructure is determined by several critical parameters, which include the temperature gradient G, solidification rate R and degree of undercooling ΔT. The ratio G/R determines the mode of solidification, while the product GR (undercooling ΔT) governs the scale of the solidification microstructure [30,31]. The energy density in Fig. 7e is much lower so that the G is much smaller, resulting in a smaller G/R and GR. Because of the small G and resulted small ΔT, the nucleation in the melt pool is comparably homogeneous and the nuclei have enough time to grow before textured grain growth dominates solidification. Equiaxed grains are thus produced and observed in Fig. 7e. With the larger G in Fig. 7f, dendrites aligned closely with the maximum heat flow direction at the solid-liquid interface achieve competitive growth during the solidification process, leading to the formation of columnar grains. Under certain solidification conditions, the growth of columnar structures is terminated with the formation of equiaxed structures. Among the boundary of two melt pools, the grains appear with equiaxed structure and larger than those in the melt pools, because of the low G and ΔT induced by the remelting effect of the subsequent laser beam scan.

The corresponding compositions of the regions presented in Figs. 6 and 7 are given in Table 2. The comparative elemental composition of Al and Zr obtained by EDS on the UV laser processed samples does not appear homogeneous, probably due to the fact that this laser affects the original sputtered Zr layer to a much larger extent than the alloy substrate. Under this hypothesis, differences in the Zr deposit would explain inhomogeneities in the Zr/Al elemental composition ratio throughout the UV laser affected coating, as found in analysis regions 1–3 indicated in Fig. 6. For the samples treated with the ns nIR laser, the constituent distribution is more uniform, as shown in Fig. 7. The composition of region 4 in the latter Figure suggests the presence of the hypoeutectic structure with superfluous ZrO_2. The laser energy input in this case is not large enough to sufficiently melt the substrate and allow formation of the Al_2O_3-ZrO_2 eutectic structure. With increased energy density in region 5, laser irradiation can induce a considerable thermal load on the substrate, enrich the molten pool with increased amounts of Al oxide and induce effective formation of the eutectic structure.

The elemental compositions determined by EDS correspond to

Table 2
Elemental composition (at. %) determined by EDS on the coatings obtained after treatment with ps UV and ns nIR pulsed lasers. Analysis regions are indicated in Figs. 6 and 7.

Site	O	Al	Zr
1	68.8	10.8	20.5
2	65.6	3.7	30.7
3	62.9	26.0	11.1
4	64.1	6.8	29.1
5	60.1	23.5	16.4

similar Al_2O_3-ZrO_2 ratios in the different sample areas measured, regardless of which laser (UV or nIR) was employed. For example, sites 1–2 and 4–5 may correspond to nearly similar chemical component mixtures. The difference between these, however, may be ascertained in their respective microstructures, where clear, effective eutectic structure formation is confirmed only in the case of an IR laser treatment, consistent with the above argument.

3.3. Phase composition

The XRD patterns in Fig. 8 summarize the evolution of the crystalline phases of the coating obtained by MAO and by SLM using the nIR laser. After a 5 min long MAO process, shown in Fig. 8a, m-ZrO_2 and t-ZrO_2 are found in the apparent absence of Al_2O_3, whose diffraction lines are not clearly detected in the lower diffraction pattern of this Figure. After the MAO process is carried out for 30 min, the coating contains t-ZrO_2 as the major crystalline phase, besides m-ZrO_2 and γ-Al_2O_3, whose main diffraction lines are observed. Similar phases have been reported for a ZrO_2 ceramic coated LY12 Al alloy [32]. During the MAO process, the local temperature of the discharge channels can reach 10^3-10^4 K, which can melt the Zr layer and result in the formation of liquid ZrO_2.

Under equilibrium conditions, with very low Al_2O_3 contents, high-temperature c-ZrO_2 forms at 2680 °C. Then c-ZrO_2 transforms first into t-ZrO_2 at 2370 °C and this phase into m-ZrO_2 at 1240 °C. The presence of c-ZrO_2 and t-ZrO_2 are not expected under equilibrium cooling conditions down to RT (room temperature or electrolytic solution temperature). Fast non-equilibrium cooling characteristic to MAO may stabilize or "freeze" metastable phases which transform via atomic diffusion. The presence of t-ZrO_2, with a higher stability temperature range than c-ZrO_2, at RT could also be consistent with specific cooling rates intrinsically related to the applied experimental MAO conditions, and the associated sub-cooling processes. Hence, it is not difficult to envisage that zirconium oxide-based compounds are subject to known phase transformations under non-equilibrium conditions, as the reaction products are in contact with cold electrolyte. The former conditions would thus explain the formation of predominately t-ZrO_2, consistent with the phase diagram of Fig. 4(a) and supported by previous published work [15]. The latter reported on the appearance of m-ZrO_2 under slow solidification rates, in contrast with t-ZrO_2, found in thermally quenched areas. Furthermore, the addition of Al_2O_3 can stabilize t-ZrO_2 under the compression exerted by the surrounding Al_2O_3 matrix [33].

The coating fabricated by SLM with a hatching distance of 5 μm exhibits a crystalline phase composition based on small amounts of t-ZrO_2, Zr_3O phases, together with that corresponding to the Al alloy substrate. This is most likely due to the fact that the coating has peeled off and exposed the bare substrate. The sample prepared with the interlinear distance of 35 μm mainly shows the structure of t-ZrO_2, but also exhibits diffraction lines corresponding to m-ZrO_2, Zr_3O, γ-Al_2O_3 and Al. The existence of Zr_3O may result from insufficient oxygen uptake combined with very fast solidification rates characteristic of this laser beam scan process. SLM can also yield t-ZrO_2, due to the thermodynamic non-equilibrium processes that are generated. The reason for the apparent formation of this phase may well be assigned to the severe conditions imposed by the laser surface process, combining very high temperatures with very high cooling rates. The t-ZrO_2 phase is thus "frozen" under very high cooling rates, avoiding, at least to a certain extent, the expected phase transition to its monoclinic allotrope [21,34].

3.4. Nano indentation

Fig. 9 shows the mean values of nano-hardness and reduced Young's modulus for samples #1 to #5. The error bars represent the standard deviation of results gathered from ten tests. The Al_2O_3-ZrO_2 layer prepared by the 30 min MAO process was selected as sample #3 here. Moreover, the Al_2O_3-ZrO_2 layer after the treatment by the near IR ns pulsed Fiber laser emitting with beam scan rate of 400 mm/s and a hatching distance of 35 μm was correspondingly taken as sample #5. It is found that the hardness of #1 (Al substrate) is about 1.21 GPa. After the deposition of Zr, the hardness of the coatings is developed in varying degrees. The hardness of the Zr layer deposited directly on 6061 Al alloy (#2) is much higher than that deposited on the Al_2O_3 layer generated by MAO (#4). The lower hardness of the coating in sample #4 may be explained by the porosity and presence of cracks within the Al_2O_3 layer underneath the Zr coating. However, after the MAO treatment on the Zr coating, the porous Al_2O_3-ZrO_2 layer in sample #3 (2.38 GPa) is harder than the dense Al_2O_3-ZrO_2 layer in sample #5, fabricated by SLM (1.67 GPa). This phenomenon may be dominated by an increased content of ZrO_2, which exhibits lower hardness than Al_2O_3 in sample #5 [35].

Fig. 9b shows the modulus of the alloy and coatings. The modulus of the Zr layer (#2) is significantly higher than the value for the 6061 Al alloy (#1), while the value of the Zr layer in sample (#4) is slightly lower. As discussed above, the porous Al_2O_3 layer underneath significantly affects the mechanical properties of the Zr layer. After the latter layer is subjected to MAO, the modulus of the Al_2O_3-ZrO_2 layer descends to 44.95 GPa, as expected from its porous structure. However, after SLM, the modulus of this coating increases to a steady value of 51.82 GPa.

The observed behaviour in hardness and modulus are similar in all the studied samples. The MAO treatment can reduce the hardness and modulus of the Zr layer through formation of a porous and cracked

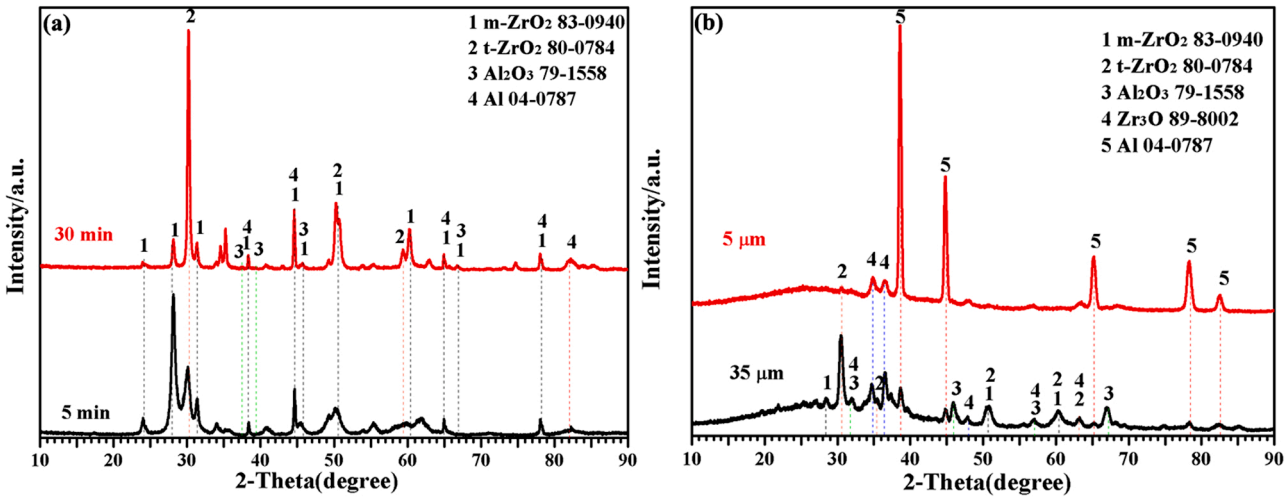

Fig. 8. XRD patterns of the Al_2O_3-ZrO_2 coatings fabricated by (a) MAO and (b) SLM.

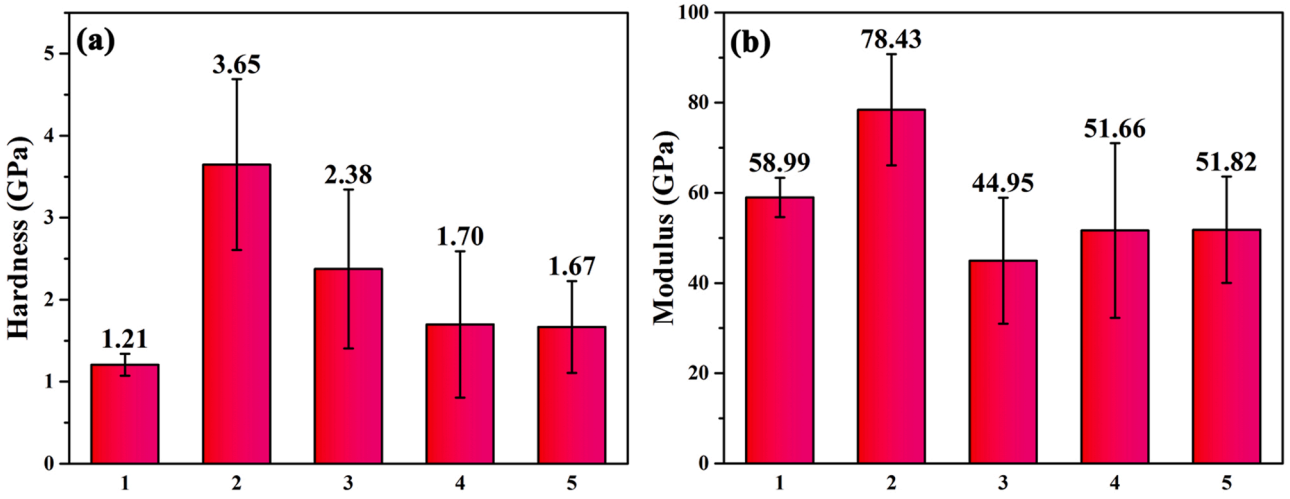

Fig. 9. (a) Hardness and (b) modulus of samples #1-#5 in Fig. 1 obtained from nano-indentation measurements.

structured Al_2O_3-ZrO_2 coating. In contrast, the bilayer structure of porous Al_2O_3 + Zr layer possesses the same hardness and modulus as the Al_2O_3-ZrO_2 coating prepared by SLM. Moreover, the Al_2O_3-ZrO_2 coating prepared by MAO exhibits a higher hardness and a somewhat lower Young's modulus compared with those obtained by SLM.

3.5. Discussion

The mechanism, process and the obtained coatings of MAO and SLM are quite different according to the above results. Thereby, the two in-situ oxidation methods are herewith compared.

Fig. 10 shows illustrative schemes of the MAO and SLM processes herein reported. In the case of MAO, cracks and pores are the natural channels through which micro-discharges take place, and the efficiency of electro-thermal conversion is thus very high. For SLM, the efficiency of photo-thermal conversion depends on the state of the material. Some of the energy is reflected and cannot be absorbed by the substrate. The holding time in this case refers to the pulse width and its influence on heat accumulation via pulse to pulse overlap. This is particularly important as the pulse repetition rate or frequency is increased above kHz values. Although very high temperatures may be reached, these are induced at or near the surface of the sample. This results in very fast cooling rates, once the laser source is turned off.

During the MAO process, there are two approaches for consumption

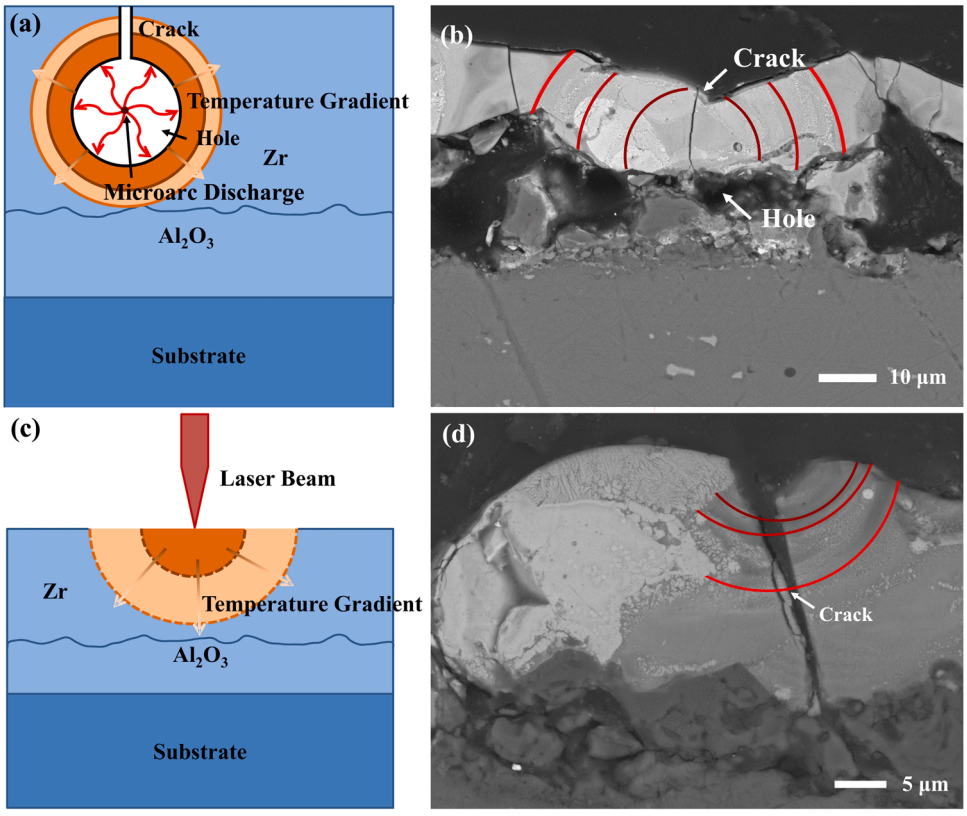

Fig. 10. Schemes of MAO (a) and SLM (c) and the typical cross-sectional morphologies of Al_2O_3-ZrO_2 coating after oxidation by MAO (b) and SLM (d), respectively, as discussed in the text.

of OH^-. When the Zr layer comes into contact with the solution, OH^- can react with Zr directly by Eqs. (2)–(3) [17]. When the upper part of the Zr layer is oxidized and MAO occurs inside the coating consequently, there are sufficient OH^- ions in the solution, of which some react with Zr^{4+} and Al^{3+}, and the others generate oxygen according to Eq. (4). Under the electric field associated to the high voltage, oxygen is ionized to oxygen plasma and then this plasma reacts with the metal ions. Moreover, most oxygen can escape as gas, yielding the holes in the coating observed in the top view of Fig. 3.

$$Zr \rightarrow Zr^{4+} + 4e^- \quad (2)$$

$$Zr^{4+} + 2OH^- + 2H_2O \rightarrow ZrO_2 + 2H_3O^+ \quad (3)$$

$$4OH^- - 4e^- \rightarrow O_2 + 2H_2O \quad (4)$$

In the case of SLM, the oxygen is taken from the atmosphere where the laser treatment is performed. When the intensity of the laser is low, the laser beam can be considered as a more conventional, localized heat source. With the increase in the laser intensity, the substrate can be melted and readily reacts with oxygen. Above a certain intensity, a plasma that can shield laser light is formed and competes with the characteristic higher absorption of this radiation at high temperatures. Besides, the reaction location depends on the operation mode of the laser.

During the melting process of the material, the highest temperature exists either in volumes where the micro-discharges occur, or at the incidence point of the laser on the surface of the sample. For MAO, micro-discharges occur in the holes that appear in the coating, while the laser is effective on the outermost surface of the sample. The temperature gradient is away from the center of the highest temperature point so that the molten zone exhibits a ball-like shape during the MAO process, whereas it is confirmed as crown type for SLM. Because the MAO process progresses in solutions, the loss of heat is much faster than in the SLM process. The soaking time is proportional to the pulse width at a constant pulse repetition rate. With laser irradiation in SLM, however, a thermal accumulation effect is associated to pulse-to-pulse overlap, increasing the temperature of the irradiated material considerably. In addition, the laser works in a beam scan mode, reheating the same zone several times, as each line described by the laser beam is overlapped by subsequent lines. As a result, the overall sample temperature decreases at a slower pace than in MAO.

The solidification interface separating the melt from adjacent colder zones at room temperature in MAO and SLM, may result initially in a fine grain size solidified crystalline solid. Owing to the maximum degree of supercooling, the initial nucleation and solidification appears at the melt boundary. Progressive solidification then occurs towards the center of the melt, with a consequent increase in grain size and Zr at. %. However, the shock waves provoked by the plasma and the laser, as well as the thermal expansion coefficient difference, may result in the appearance of structural defects, such as microcracks, during such processes. Future progress in these methodologies will require increased knowledge of the complex phenomena involved in MAO and SLM processes, as well as improved conditions to avoid the formation of micro and macroscopic defects, which deprive the final products obtained from reaching optimum properties.

4. Conclusion

This work reports on the in-situ oxidation behavior of Zr deposited on 6061 aluminum alloy by MAO, as well as on an Al_2O_3 MAO-coated 6061 aluminum substrate by SLM. Morphologies, crystalline phase composition and nano-indentation were studied and the difference between the two processing methods were compared. It was found that:

Al_2O_3-ZrO_2 coating is obtained by MAO and SLM processes. The coating prepared by MAO displays a porous structure because of the micro-arc discharge in the insulating film. The SLM process results in a denser coating, although with the presence of cracks arising from thermomechanical stresses.

The crystalline phases found within the MAO treated coating are confirmed to be m-ZrO_2, t-ZrO_2 and γ-Al_2O_3. The coating prepared by SLM, with a hatching interlinear distance of 35 μm, exhibits mainly the structure of t-ZrO_2, m-ZrO_2, Zr_3O and γ-Al_2O_3, where the existence of Zr_3O may result from insufficient exposure to oxygen during the fast heating/solidifying process intrinsic to this method.

The Al_2O_3-ZrO_2 coating prepared by MAO exhibits a higher hardness and a lower Young's modulus compared with that obtained by SLM. This difference is ascribed to the porous structure of the Al_2O_3-ZrO_2 coating prepared by MAO.

Declaration of Competing Interest

The authors declare that they have no known competing financial interests or personal relationships that could have appeared to influence the work reported in this paper.

Acknowledgements

The authors gratefully acknowledge the financial support of the project from the National Natural Science Foundation of China (No. 51571114, 51401106) and the Priority Academic Program Development of Jiangsu Higher Education Institutions (PAPD), from the Spanish MCIN/AEI/10.13039/501100011033 (project PID2020-113034RB-I00) and from Gobierno de Aragón (research group T54_20R). Authors would like to acknowledge the use of Servicio General de Apoyo a la Investigación-SAI, Universidad de Zaragoza.

References

[1] W. Xue, Q. Zhu, Q. Jin, M. Hua, Characterization of ceramic coatings fabricated on zirconium alloy by plasma electrolytic oxidation in silicate electrolyte, Mater. Chem. Phys. 120 (2010) 656–660, https://doi.org/10.1016/j.matchemphys.2009.12.012.

[2] H. Tang, Q. Sun, C.G. Yi, Z.H. Jiang, F.P. Wang, High emissivity coatings on titanium alloy prepared by micro-arc oxidation for high temperature application, J. Mater. Sci. 47 (2012) 2162–2168, https://doi.org/10.1007/s10853-011-6017-3.

[3] F. Monfort, A. Berkani, E. Matykina, P. Skeldon, G.E. Thompson, H. Habazaki, K. Shimizu, Development of anodic coatings on aluminium under sparking conditions in silicate electrolyte, Corros. Sci. 49 (2007) 672–693, https://doi.org/10.1016/j.corsci.2006.05.046.

[4] A.L. Yerokhin, X. Nie, A. Leyland, A. Matthews, Characterisation of oxide films produced by plasma electrolytic oxidation of a Ti-6Al-4V alloy, Surf. Coat. Tech. 130 (2000) 195–206, https://doi.org/10.1016/S0257-8972(00)00719-2.

[5] W. Xue, Z. Deng, Y. Lai, R. Chen, Analysis of phase distribution for ceramic coatings formed by microarc oxidation on aluminum alloy, J. Am. Ceram. Soc. 81 (1998) 1365–1368, https://doi.org/10.1111/j.1151-2916.1998.tb02493.x.

[6] W. Xue, C. Wang, Y. Li, Z. Deng, R. Chen, T. Zhang, Effect of microarc discharge surface treatment on the tensile properties of Al-Cu-Mg alloy, Mater. Lett. 56 (2002) 737–743, https://doi.org/10.1016/S0167-577X(02)00605-5.

[7] S.V. Gnedenkov, P.S. Gordienko, O.A. Khrisanfova, T.M. Scorobogatova, S. L. Sinebrukhov, Formation of $BaTiO_3$ coatings on titanium by microarc oxidation method, J. Mater. Sci. 37 (2002) 2263–2265, https://doi.org/10.1023/A:1015317316363.

[8] A.L. Yerokhin, L.O. Snizhko, N.L. Gurevina, A. Leyland, A. Pilkington, A. Matthews, Spatial characteristics of discharge phenomena in plasma electrolytic oxidation of aluminium alloy, Surf. Coat. Tech. 177 (2004) 779–783, https://doi.org/10.1016/j.surfcoat.2003.06.020.

[9] Y. Ma, X. Nie, D.O. Northwood, H. Hu, Systematic study of the electrolytic plasma oxidation process on a Mg alloy for corrosion protection, Thin Solid Films 494 (2006) 296–301, https://doi.org/10.1016/j.tsf.2005.08.156.

[10] Y. Chen, Y. Yang, Z. Chu, X. Chen, L. Wang, Z. Liu, Y. Dong, D. Yan, J. Zhang, Z. Kang, Microstructure and properties of Al_2O_3-ZrO_2 composite coatings prepared by air plasma spraying, Appl. Surf. Sci. 431 (2018) 93–100, https://doi.org/10.1016/j.apsusc.2017.04.073.

[11] V. Shoaei-Rad, M.R. Bayati, H.R. Zargar, J. Javadpour, F. Golestani-Fard, In situ growth of ZrO_2-Al_2O_3 nano-crystalline ceramic coatings via micro arc oxidation of aluminum substrates, Mater. Res. Bull. 47 (2012) 1494–1499, https://doi.org/10.1016/j.materresbull.2012.02.031.

[12] B. Qian, Z. Shen, Laser sintering of ceramics, J. Asian Ceram. Soc. 1 (2013) 315–321, https://doi.org/10.1016/j.jascer.2013.08.004.

[13] V.V. Lennikov, J.M. Pedra, J.J. Gómez, G.F. de la Fuente, J.B. Carda, In situ synthesis of composite $MTiO_3$-Al_2O_3 coatings via laser zone melting, Solid State Sci. 9 (2007) 404–409, https://doi.org/10.1016/j.solidstatesciences.2007.03.013.

[14] I. de Francisco, V.V. Lennikov, J.A. Bea, A. Vegas, J.B. Carda, G.F. de la Fuente, In-situ laser synthesis of rare earth aluminate coatings in the system *Ln*-Al-O (*Ln* = Y, Gd), Solid State Sci. 13 (2011) 1813–1819, https://doi.org/10.1016/j.solidstatesciences.2011.07.013.

[15] A. Larrea, G.F. de la Fuente, R.I. Merino, V.M. Orera, ZrO_2-Al_2O_3 eutectic plates produced by laser zone melting, J. Eur. Ceram. Soc. 22 (2002) 191–198, https://doi.org/10.1016/S0955-2219(01)00279-5.

[16] F. Niu, D. Wu, G. Ma, J. Wang, M. Guo, B. Zhang, Nanosized microstructure of Al_2O_3-ZrO_2 (Y_2O_3) eutectics fabricated by laser engineered net shaping, Scr. Mater. 95 (2015) 39–41, https://doi.org/10.1016/j.scriptamat.2014.09.026.

[17] V. Shaei-Rad, M.R. Bayati, F. Golestani-Fard, H.R. Zargar, J. Javadpour, Fabrication of ZrO_2-Al_2O_3 hybrid nano-porous layers through micro arc oxidation process, Mater. Lett. 65 (2011) 1835–1838, https://doi.org/10.1016/j.matlet.2011.03.086.

[18] M. Le Saux, T. Guilbert, J.C. Brachet, An approach to study oxidation-induced stresses in Zr alloys oxidized at high temperature, Corros. Sci. 140 (2018) 79–91, https://doi.org/10.1016/j.corsci.2018.06.016.

[19] S.M. Lakiza, L.M. Lopato, Stable and metastable phase relations in the system alumina-zirconia-yttria, J. Am. Ceram. Soc. 80 (1997) 893–902, https://doi.org/10.1111/j.1151-2916.1997.tb02919.x.

[20] O. Fabrichnaya, F. Aldinger, Assessment of thermodynamic parameters in the system ZrO_2-Y_2O_3-Al_2O_3, Z. Metallkd. 95 (2004) 27–39, https://doi.org/10.3139/146.017909.

[21] J.M. Calderón-Moreno, M. Yoshimura, Stabilization of zirconia lamellae in rapidly solidified alumina-zirconia eutectic composites, J. Eur. Ceram. Soc. 25 (2005) 1369–1372, https://doi.org/10.1016/j.jeurceramsoc.2005.01.013.

[22] J. Wang, C. Weng, J. Chang, C. Hwang, The influence of temperature and surface conditions on surface absorptivity in laser surface treatment, J. Appl. Phys. 87 (2000) 3245–3253, https://doi.org/10.1063/1.372331.

[23] H. Wang, Y. Kawahito, R. Yoshida, Y. Nakashima, K. Shiokawa, A model to calculate the laser absorption property of actual surface, Int. J. Heat. Mass Tran. 118 (2018) 562–569, https://doi.org/10.1016/j.ijheatmasstransfer.2017.11.023.

[24] E. Akman, Y. Erdoğan, M.Ö. Bora, O. Çoban, B.G. Oztoprak, A. Demir, Investigation of the differences between photochemical and photothermal laser ablation on the shear strength of CFRP/CFRP adhesive joints, Int. J. Adhes. Adhes. 98 (2020), 102548, https://doi.org/10.1016/j.ijadhadh.2020.102548.

[25] A. Cubero, E. Martínez, L.A. Angurel, G.F. de la Fuente, R. Navarro, H. Legall, J. Krüger, J. Bonse, Surface superconductivity changes on niobium sheets by femptosecond laser-induced periodic nanostructures, Nanomater 10 (2020) 2525, https://doi.org/10.3390/nano10122525.

[26] I. de Francisco, J.A. Bea, A. Vegas, J.B. Carda, G.F. de la Fuente, In-situ laser synthesis of Nd-Al-O coatings: the role of sublattice cations in eutectic formation, Acta Crystallogr. B 71 (2015) 95–111, https://doi.org/10.1107/S2052520615000864.

[27] F. Rey-García, F. Gutiérrez-Mora, C.J. Borrel, L.C. Estepa, L.A. Angurel, G.F. de La Fuente, Microstructural characterization and tribological behavior of Laser Furnace processed ceramic tiles, Ceram. Int. 44 (2018) 6997–7005, https://doi.org/10.1016/j.ceramint.2018.01.133.

[28] D.D. Gu, W. Meiners, K. Wissenbach, R. Poprawe, Laser additive manufacturing of metallic components: materials, processes and mechanisms, Int. Mater. Rev. 57 (2012) 133–164, https://doi.org/10.1179/1743280411Y.0000000014.

[29] M. Mora, J.C. Díez, C.I. López-Gascón, E. Martínez, G.F. de la Fuente, Laser textured Bi-2212 in planar geometries, IEEE T. Appl. Supercon. 13 (2003) 3188–3191, https://doi.org/10.1109/TASC.2003.812192.

[30] M. Flemings, Solidification Processing, McGraw-Hill, Inc, New York, 1974. ISBN 0-07-021283-x.

[31] T. DebRoy, H.L. Wei, H.S. Zuback, T. Mukherjee, J.W. Elmer, J.O. Milewski, A. M. Beese, A. Wilson-Heid, A. De, W. Zhang, Additive manufacturing of metallic components - process, structure and properties, Prog. Mater. Sci. 92 (2018) 112–224, https://doi.org/10.1016/j.pmatsci.2017.10.001.

[32] Z. Wu, Z. Yao, Z. Jiang, Preparation and structure of microarc oxidation ceramic coatings containing ZrO_2 grown on LY12 Al alloy, Rare Met. 27 (2008) 55–58, https://doi.org/10.1016/S1001-0521(08)60030-3.

[33] Y. Yan, Y. Han, J. Huang, Formation of Al_2O_3-ZrO_2 composite coating on zirconium by micro-arc oxidation, Scr. Mater. 59 (2008) 203–206, https://doi.org/10.1016/j.scriptamat.2008.03.015.

[34] Z. Wang, J. Ouyang, Y. Wang, L. Xie, Y. Ma, Z. Liu, A. Henniche, Y. Wang, Microstructural characterization of nanostructured Al_2O_3-ZrO_2 eutectic layer by laser rapid solidification method, Appl. Surf. Sci. 476 (2019) 335–341, https://doi.org/10.1016/j.apsusc.2019.01.096.

[35] M. Moazzam Hossen, F.-U.-Z. Chowdhury, M.A. Gafur, A.K.M. Abdul Hakim, Structural and mechanical properties of zirconia toughened alumina (ZTA), Compos., Int. J. Eng. Res. Tech. 3 (2014) 2128–2134.